Research Square

Preprints are preliminary reports that have not undergone peer review.
They should not be considered conclusive, used to inform clinical practice,
or referenced by the media as validated information.

A Generalized Theory of Ion Conductivity in Nanoporous Media

Mohammad Javad Abdolhosseini Qomi

m.jaq@uci.edu

University of California, Irvine https://orcid.org/0000-0001-6911-0994

Jerry Peprah Owusu

University of California, Irvine https://orcid.org/0000-0003-3808-0264

Kevin Rosso

Pacific Northwest National Laboratory https://orcid.org/0000-0002-8474-7720

Russell Detwiler

University of California, Irvine

Article

Keywords:

Posted Date: April 2nd, 2026

DOI: https://doi.org/10.21203/rs.3.rs-9238623/v1

License: This work is licensed under a Creative Commons Attribution 4.0 International License.
Read Full License

Additional Declarations: There is **NO** Competing Interest.

A Generalized Theory of Ion Conductivity in Nanoporous Media

Jerry P. Owusu[1], Kevin M. Rosso[2], Russell L. Detwiler[1],
and Mohammad Javad Abdolhosseini Qomi[1,3,4*]
[1]*Department of Civil and Environmental Engineering, University of California, Irvine, CA 92697, USA.*
[2]*Physical and Computational Sciences Directorate, Pacific Northwest National Laboratory, Richland, WA, USA.*
[3]*Department of Materials Science and Engineering, University of California, Irvine, CA 92697, USA. and*
[4]*Department of Mechanical and Aerospace Engineering, University of California, Irvine, CA 92697, USA.*

ABSTRACT

Ion conductivity in nanoporous media underpins energy storage, water purification, materials characterization, and subsurface sensing, yet classical transport theories fail at the nanoscale by neglecting interfacial phenomena. Using high-throughput non-equilibrium molecular dynamics with a reduced-complexity surface-chemistry model, we systematically vary pore size, surface charge, and ion affinity, and apply an electric field to probe nanoscale ion dynamics from zero-field diffusion to strongly driven conduction. This reveals three distinct dynamical regimes: confinement-driven linear response in charge-neutral pores, trap-and-hop nonlinear response in charged nanopores, and an interfacial superionic regime characterized by collective ion migration along percolation networks. We propose an extended Nernst–Einstein relation that unifies these diverging transport regimes through dimensional homogeneity, validated against all-atom simulations and experimental data. This development links interfacial physics to emergent ion-transport properties, thereby providing physics-based constitutive relations for nanoporous media.

* E-mail: mjaq@uci.edu

The ability to control and predict the movement of ions through nanoscale spaces underpins many technologies central to modern science and engineering. In energy storage devices, such as supercapacitors and batteries, ion transport within nanostructured electrodes determines capacity, rate performance, and long-term stability [1–3]. Similar mechanisms govern the efficiency of water desalination and ion-selective membranes, where ion motion through narrow channels controls both selectivity and throughput [4, 5]. Confinement effects, such as partial dehydration, steric hindrance, and electrostatic interactions, enable precise ion selectivity, supporting applications ranging from critical mineral recovery to pharmaceutical purification [6–9]. Likewise, in electrical sensing of infrastructure and geosystems, impedance measurements depend on models that link pore-scale ion dynamics to bulk electrical response [10–13]. Across these diverse systems, a common challenge emerges: traditional theories developed for bulk electrolytes cannot fully account for the ion behavior in nanoconfined spaces.

At the core of this challenge lies the Nernst-Einstein relation, the foundational law for ionic conductivity that assumes ion dynamics remain unaffected by their local environment [14]. This holds in large pores but fails as confinement approaches the molecular scale. In nanoporous carbon electrodes, ion desolvation and correlations produce anomalous capacitance beyond bulk models [3, 15, 16]. Carbon nanotube porins and silicon nitride nanochannels show transport breaking down by orders of magnitude [6, 17, 18]. These deviations arise from confinement-altered fluid structure [6], electrostatic coupling between surface charges and the electrolyte [19, 20], and ion-specific adsorption at solid-fluid interfaces [21–23]. Below $\sim$ 10 nm, interfacial physics, such as surface-charge electrostatics, modified solvation, and ion–ion correlations, dominate ion mobility. Bulk-based laws are thus inadequate for nanoporous materials [6, 24, 25].

While the microscopic origins of interfacial phenomena are well established, their collective impact on macroscopic electrical behavior remains poorly constrained. Advancing beyond bulk-based scaling, therefore, requires a framework that couples molecular-scale ion dynamics with the emergent transport properties of nanoporous media. Such a framework must decouple intrinsic ion mobility from geometric connectivity and reformulate the Nernst–Einstein relation to account for the altered diffusivity and electrostatic environment under confinement. Establishing this connection between interfacial physics and effective conductivity would enable a predictive description of electrical transport that remains valid across scales and testable against experimental observations.

We employ high-throughput non-equilibrium MD simulations with a simplified surface-chemistry

model to study nanoconfined electrolyte mobility under externally applied electric fields. In these simulations, we systematically vary pore size, surface charge, ion affinity, and field strength and examine how these parameters govern ion partitioning, drift velocity, and diffusion in neutral and charged slit nanopores, from zero-field diffusion to strongly driven conduction. Distinct conductivity regimes emerge as ions respond to confinement and surface interactions, and we identify their molecular origins to build a unified theoretical framework that explains the full range of pore-scale conductivity behaviors.

RESULTS AND DISCUSSION

A. Atomistic Setup to Study Nanoconfined Ion Conductivity: To probe nanoscale ion conduction, we construct a reduced-complexity slit nanopore that resolves atomic trajectories via classical molecular dynamics (MD) simulations (*Methods* A, B). A confined 1 M electrolyte interacts with the simplified nanopore through dispersive and electrostatic interactions. The fluid experiences an external electric field E parallel to the pore surface, causing cations and anions to drift in opposite directions. This reduced-complexity setup resolves the nanofluidic region as a function of pore width H and surface ionophilicity ϵ_s. These parameters span the range of confinement strengths and ion–surface affinities relevant to nanoporous surfaces (**Fig. 1a–c**). ϵ_s quantifies the effective ion–surface interaction, controlling ion partitioning between the bulk-like pore region and the interfacial adsorbed layers. Similarly, water-surface interactions govern the system's hydrophilicity, which we find to be strongly proportional to ϵ_s. Thus, increasing ϵ_s monotonically increases the maximum H_2O and Na^+ densities in the Stern layer (see **Fig. 1d** and Fig. S1–S2).

To connect this parameter space to realistic interfaces encountered in nanoporous systems, we calibrate ϵ_s against all-atom simulations of 1 M NaCl confined between atomistically resolved mineral surfaces, including quartz, pyrophyllite, calcite, forsterite (Σ_s=0.0, 2.0 e/nm^2), and montmorillonite (Σ_s=2.0 e/nm^2). Matching the maximum interfacial Na^+ densities between all-atom and reduced-complexity models yields consistent electrolyte densities across mineral surfaces and their equivalent coarse-grained counterparts at equivalent ϵ_s (Fig. 1e). This demonstrates that the ionophilicity parameter can potentially serve as a first-order approximation of diverse surface chemistries.

B. Linear Ion Conductivity Regime in Neutral Nanopores: To determine ion mobility in uncharged nanopores, we calculate the average ion drift velocity along each MD trajectory, $\tilde{v_d}$. The

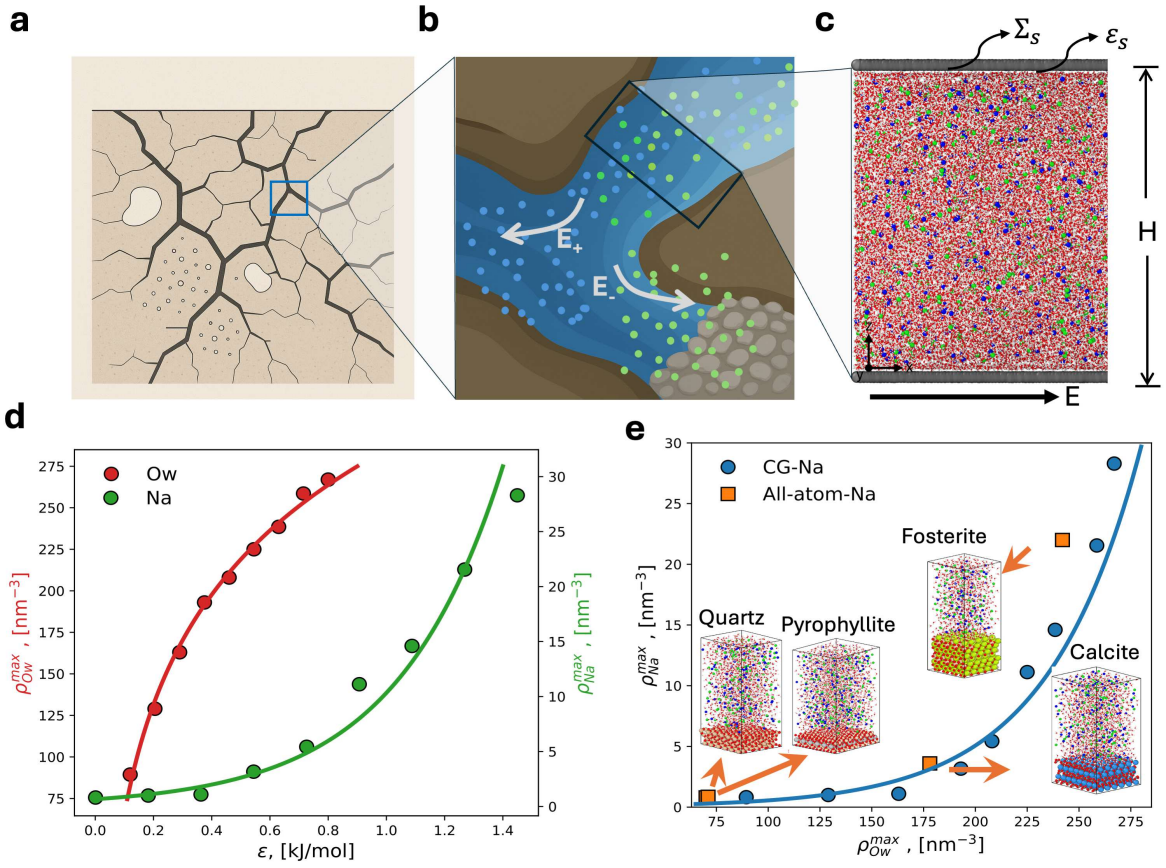


FIG. 1. **A multiscale framework for ion conductivity in nanoporous media**. When an external electric field is applied to (**a**) mesoporous media, (**b**) ions preferentially migrate, resulting in an effective electric current. To capture the nanofluidic transport regimes, we set up (**c**) reduced-complexity MD simulations, in which confined electrolyte species are atomistically resolved between idealized surfaces that engender ionophilicity and surface charge. The dark gray balls are coarse-grained surface species, red balls are oxygen, white represents hydrogen, navy blue shows sodium, and green identifies chlorine ions. By systematically varying the ionophilicity parameter, we can adjust the (**d**) Maximum interfacial water and Na^+ densities. We find (**e**) coarse-grained and all-atom simulations give consistent Na^+ surface densities across neutral and charged surfaces, indicating that ionophilicity and charge capture the essential surface chemistry. In the inset images, gray represents aluminum, dark gray represents carbon, lemon green represents magnesium, orange represents silicon, blue represents calcium, and electrolyte species are shown as before.

drift velocity is directly proportional to the ion conductivity as: $\kappa = nz_i\tilde{v_d}/E$, where κ represents the ion conductivity, n denotes charge number density, and z_i is the ion charge. In total, we perform 643 MD simulations to systematically vary H, ϵ_s, and E. We confirm that $\tilde{v_d}$ remains strictly linear with the applied E (**Fig. 2a**). This observation confirms that transport remains within the linear-response regime despite large applied electric fields. More importantly, we find that $\tilde{v_d}$ decreases as H

decreases and ϵ_s increases, reflecting pronounced confinement effects. In the absence of confinement, *i.e.,* the bulk aqueous electrolyte, MD simulations show the ion conductivity follows the Nernst-Einstein relation, $\tilde{v_d} = q_i E D_0 / k_B T$, where q_i is the ionic charge, D_0 is the self-diffusion coefficient, and $k_B T$ is thermal energy. Under confinement, $\tilde{v_d}$ deviates from bulk to surface-dominated ion transport regime, where ions partition between mobile bulk-like and strongly adsorbed interfacial regions [21] (*Supplementary Note* I).

To identify the minimal set of dimensionless variables governing ion transport, we use dimensional homogeneity. The following physical quantities govern nanoconfined ion conductivity in charge-neutral pores: the bulk self-diffusion coefficient D_0, ion charge q_i, applied electric field E, nanopore width H, surface ionophilicity ϵ_s, ion-surface equilibrium distance σ_s, and thermal energy $k_B T$. *Supplementary Note* II-III explains the procedure we adopt to construct dimensionless groups that capture the essential physics of confined electrolytes. Based on this analysis, we propose the following generalized ion transport relation for charge-neutral slit nanopores:

$$\frac{\tilde{v_d} k_B T}{q_i E D_0} = \mathcal{F}\left(\epsilon_s^* = \frac{\epsilon_s}{k_B T}, \sigma_s^* = \frac{\sigma_s}{2H}\right) \tag{1}$$

where the universal function $\mathcal{F}$ encapsulates surface energetics through the dimensionless interaction strength ϵ_s^* and geometric confinement σ_s^*. In the limit of negligible confinement and weak interfacial interactions, $\mathcal{F}$ should approach unity, recovering the Nernst-Einstein relation. It is apparent from Equation 1 that function $\mathcal{F}$ acts as a scaling factor that tunes D_0 to an equivalent pore diffusion coefficient, D_p. In other words, the Nernst-Einstein formulation retains its original form, but D_0 should be replaced with D_p, $\tilde{v_d} = \frac{q_i E}{k_B T} D_p$. Therefore, we hypothesize that D_p is the fundamental transport parameter governing the nanoconfined ion conductivity.

Prior approaches relate D_p to D_0 via geometric factors and hydrodynamic slip-length corrections [26, 27]. While Saugey *et al.* adopted a continuum dielectric medium to study nanoconfined diffusion, Simonin *et al.* considered a simplified Lennard-Jones solvent that neglects the rich electrolyte chemistry. As a result, the proposed corrections overestimate D_p and fail to capture ion transport at strong interfacial affinity. To address these limitations, we derive an analytical expression for D_p (see *Methods* C for derivation). Our theory explicitly incorporates ionophilicity and size effects through two contributions: a confinement correction (Γ_c) that captures steric exclusion and hydrodynamic resistance, and a surface correction term (Γ_s) that quantifies thermally activated ion desorption from the surface. Therefore, we can analytically express D_p as follows:

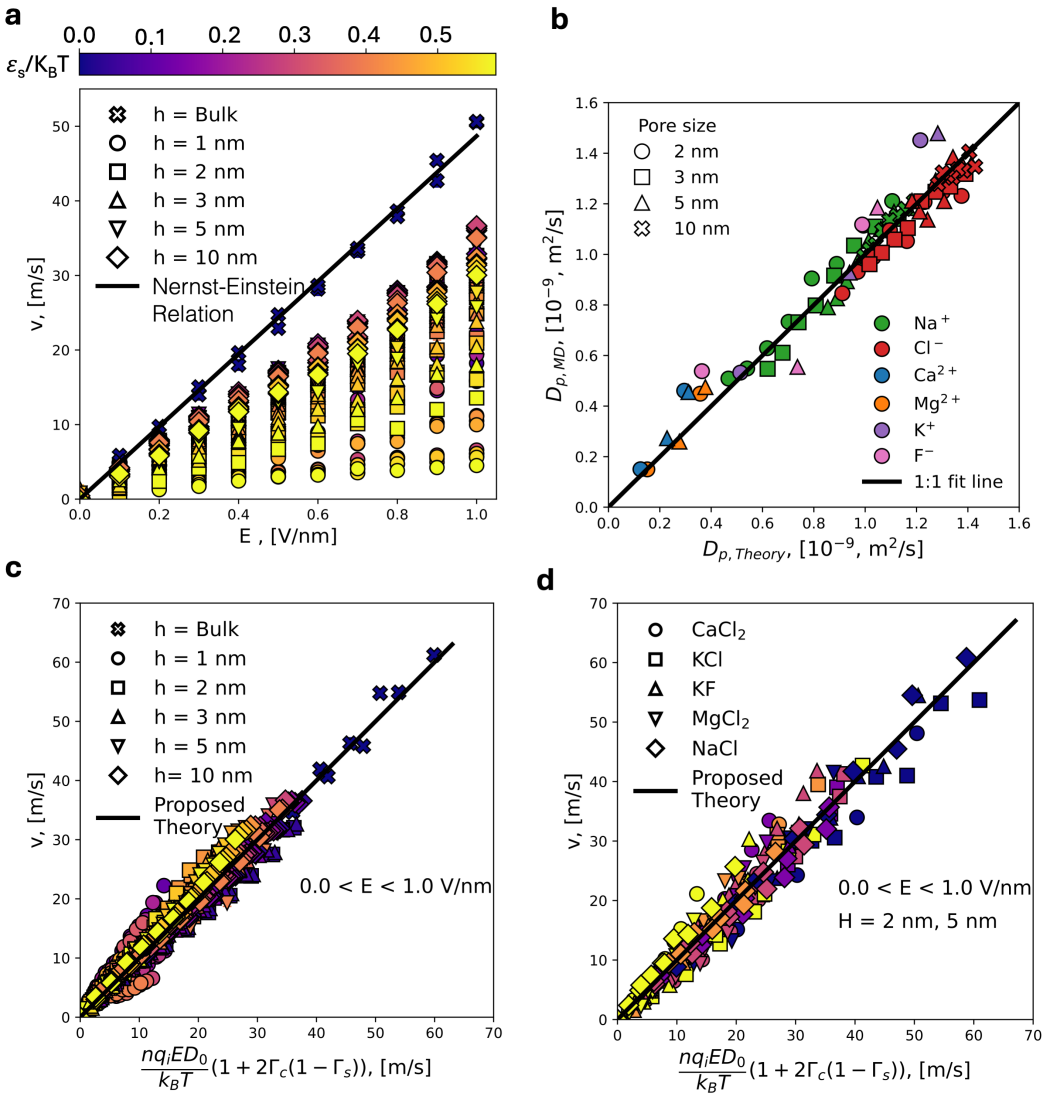


FIG. 2. **Ion transport in charge-neutral nanopores follows an ohmic behavior that breaks the Nernst-Einstein relation**. (**a**) Drift velocities from all reduced-complexity simulations show significant scatter across pore sizes and surface ionophilicities but remain strictly linear with respect to the applied external electric field. These pore size and ionophilicity effects are essentially reflected in (**b**) pore diffusion coefficients that match our theoretical predictions for different ion types. Our proposed ion conductivity theoretical framework collapses the average drift velocities for all pore sizes and surface affinities onto a master curve for (**c**) NaCl electrolyte and (**d**) other electrolytes, confirming the broad application of the proposed scaling relationship.

$$D_p = D_0(1 + 2\Gamma_c(1 - \Gamma_s)) \tag{2}$$

where $\Gamma_c = a_0\sigma_s^* ln(\sigma_s^*)$ and $\Gamma_s = \exp(-\epsilon_s^*)$. We determine the tuning parameter a_0 ≈3.0 from the ensemble of MD simulations (**Fig. 2b**). We now compare D_p calculated using the proposed theory

with that obtained directly from MD simulations via the mean-square displacement approach. The MD calculations align closely with our theoretical predictions without requiring an adjustment to a_0. We incorporate D_p into the generalized average drift velocity expression:

$$\tilde{v}_d = \frac{nq_iE}{k_BT} D_0(1 + 2\Gamma_c(1 - \Gamma_s)) \tag{3}$$

where the prefactor n represents diffusivity anisotropy, with simulations yielding $n = 2/3$ for $1 \leq H \leq 10$ nm and $n = 1/3$ for $H \leq 1$ nm . At $H \leq 1$ nm, the bulk region disappears, and ions become fully confined by the two surfaces.

With this quantitative predictive capability, we can test our hypothesis that nanoconfined diffusion is central to ion mobility under an external electric field. In fact, the proposed theory collapses drift velocities from all MD simulations onto a single master curve, proving our underlying hypothesis (**Fig. 2c**). Furthermore, we test the transferability of our model beyond the NaCl electrolyte and evaluate it on four additional electrolytes. Despite divalent cations exhibiting a stronger surface-binding affinity than monovalent ions, the proposed theory remains transferable (**Fig. 2d**). Consistent with this picture of surface-controlled mobility, interfacial Na^+ on neutral surfaces exhibits partial dehydration and rapidly exchanging hydration shells ($CN \approx 4.6$–4.9, $\tau_m \approx 15$–54 ps (*Supplementary Note* IV, Fig. S3), indicating that adsorption involves dynamically mixed inner- and outer-sphere complexes rather than strongly locked solvation structures. While the proposed theory remains valid in the limit of charge-neutral surfaces, it becomes increasingly invalid for charged surfaces.

C. Nonlinear Ion Conductivity Regime in Charged Nanopores: Surface charge restructures ion transport energy landscapes by introducing charged sites, q_s, that strongly adsorb ions [19, 21, 28]. Our reduced-complexity models introduce a surface charge density Σ_s by distributing negative charge q_s at intervals of $Delta = 0.5$ nm along the surface. As with neutral nanopores, we apply an external electric field parallel to the pore surface and compute the average drift velocity. We find that in charged nanopores, $\tilde{v_d}$ deviates significantly from the proposed linear behavior (see **Fig. 3a,b** for low- and high-ionophilic surfaces, respectively). Deviations are minimal at low surface charge and weak ionophilicity **Fig. 3a**, but drift velocity rises sharply in higher surface charge and strong ionophilic surfaces, **Fig. 3b**. The average drift velocity of Cl^- anions remains nearly linear due to the cushioning effect of electrostatic repulsion that keeps anions away from the Stern layer (Fig. S4). Nevertheless, the observed Na^+ drift nonlinearity reflects a distinct transport mechanism beyond the neutral-pore confinement model proposed in Eq. 3.

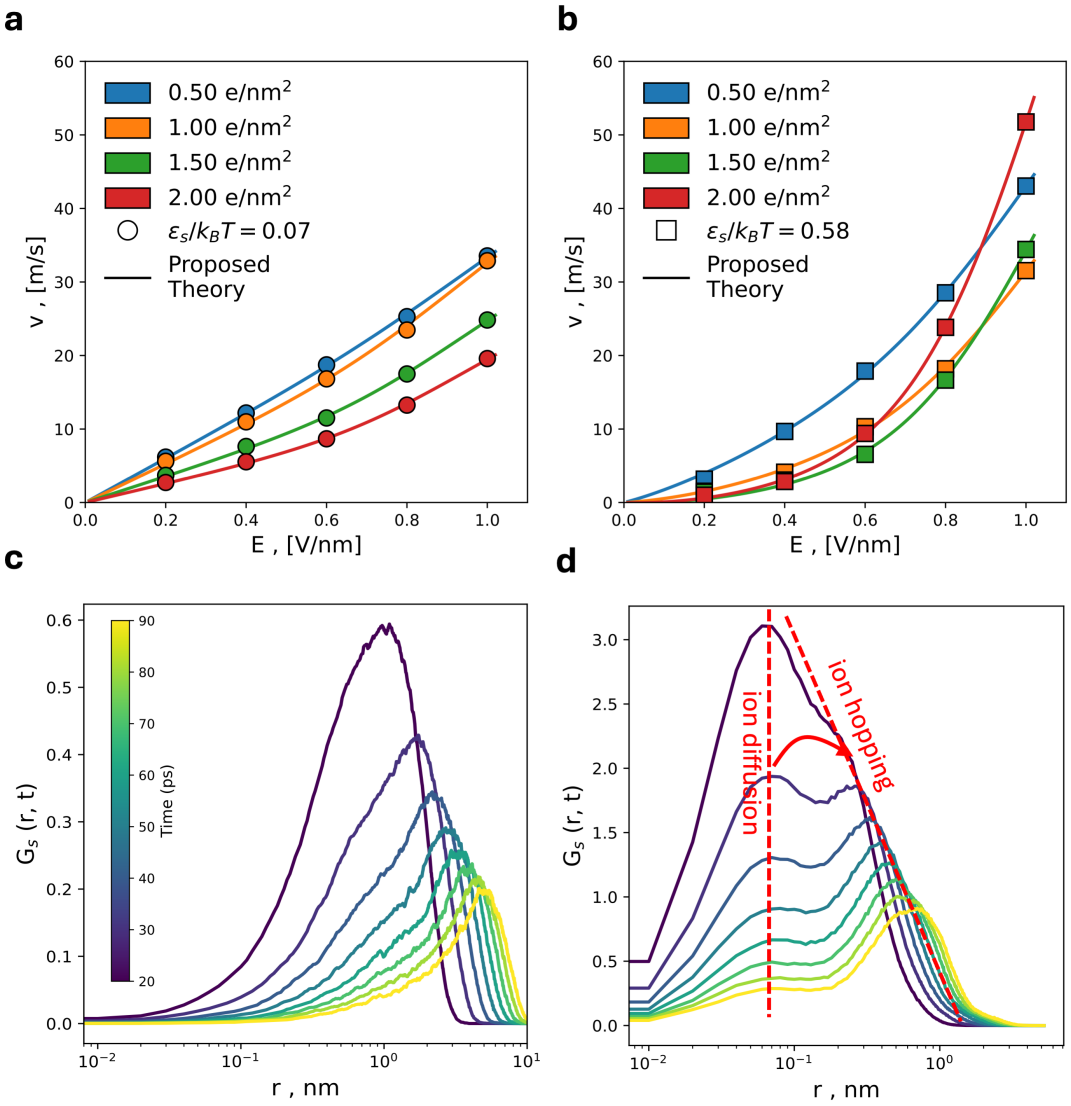


FIG. 3. **Cation transport in negatively charged nanopores follows a nonlinear behavior characterized by a hopping mechanism between surface trap sites**. This nonlinearity increases with ϵ_s^* and Σ_s for the average drift velocity versus the electric field. It becomes less noticeable for (a) low ionophilicity, ϵ_s^*=0.07, but more pronounced for (b) high ionophilicity, ϵ_s^*=0.58. The Van Hove space-time correlation reveals the molecular origins of this hopping mechanism, $G_s(r,t)$, where (c) charged-neutral pores exhibit smooth Gaussian profiles indicative of continuous diffusive motion and (d) charged pores show distinct peaks at characteristic hopping distances signaling a transition to trap-assisted transport.

We clarify the molecular origins of the observed nonlinearity by probing the Van Hove space-time correlation function $G_s(r,t)$ that traces ion displacement distributions over time from their initial position (*Methods* D and *Supplementary Note* V, Fig. S5-S6). Neutral pores show a single broadening peak reflecting normal diffusion with transient, uncorrelated surface interactions (**Fig. 3c**). Charged

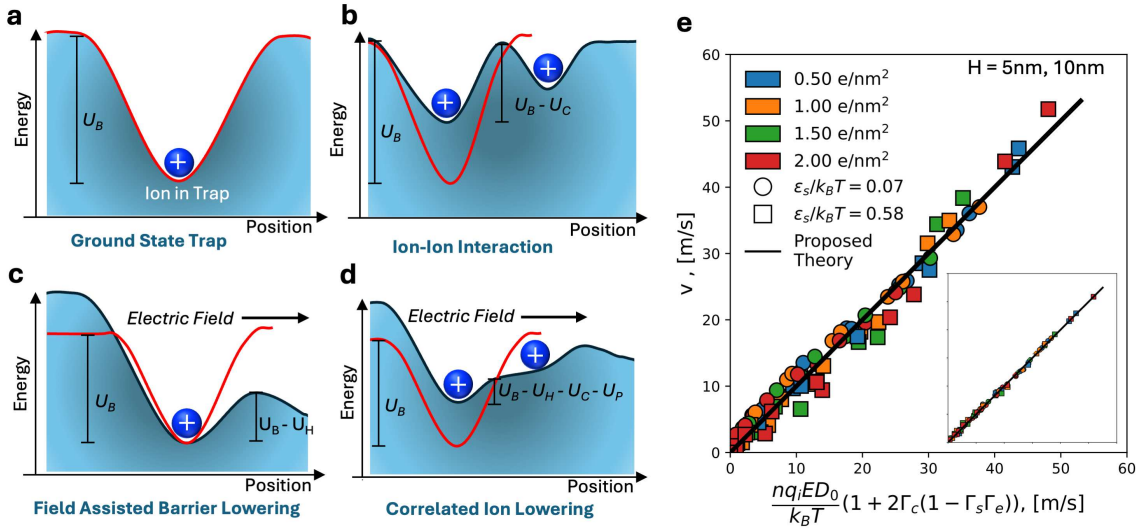


FIG. 4. **The energy barrier landscape of adsorbed ions on trap sites is at the origins of the observed nonlinear ion transport mechanisms**. (a) Surface charge sites create electrostatic traps of depth U_B that immobilize counterions. (b) At sufficiently large surface charges, charge-charge and charge-dipole crowding reduce the effective trap depth by U_C. (c) An applied electric field tilts the energy barrier potential in the direction of the applied field and lowers the forward barrier by U_H, promoting field-assisted escape. (d) Collective ion-ion correlations in percolation networks further reduce barriers by U_P, enabling rapid lateral transport along connected pathways. At the limit of negligible ion crowding and correlation effects (e), the proposed theoretical framework for charged surfaces accurately collapses average drift velocities onto the unity line. The inset shows the perfect fit when crowding and ion-correlation effects are accounted for (see discussion in *Supplementary Note* V.

pores, however, exhibit a bimodal profile: a small-displacement peak from ions trapped in electrostatic wells and a second peak at ~ 0.5 nm matching charge-site spacing (**Fig. 3d**). This bimodal structure persists for up to 90 ps, confirming that a thermally activated trap-and-hop transport mechanism replaces continuous diffusion at the interface.

To develop a theoretical framework to rationalize this nonlinearity, we revisit our dimensional analysis presented in Eq. 1 and include the physical parameters that alter ion transport processes from the energy-landscape perspective (**Fig. 4.a-d**). In addition to q_s and Δ, these physical parameters include the medium's permittivity ϵ, the electrolyte Debye screening length λ_D, and the escape distance Δ/d that a cation needs to travel to reach the saddle point in the energy landscape. We can thus extend our dimensional analysis to include charged slit nanopores as follows:

$$\frac{\tilde{v_d} k_B T}{q_i E D_0} = \mathcal{F}\left(\epsilon_s^*, \sigma_s^*, \lambda_D^* = \frac{\lambda_D}{H}, U_B^* = \frac{d q_i q_s}{4\pi\epsilon\Delta k_B T}, U_H^* = \sqrt{\frac{q_i^2 q_s E_e}{\pi\epsilon(k_B T)^2}}, q* = \frac{q_i}{q_s}\right) \tag{4}$$

where the size effect λ_D^* signifies the possibility of electric double-layer overlap in the limit of small concentrations that is negligible in the range of pore size and concentration considered in this work (*Supplementary Note* III).

In the absence of an external electric field, negatively charged sites create Coulombic wells of depth U_B^*, which immobilize cations with thermally-limited escape (**Fig. 4.a**). Additionally, in charged nanopores, charge–charge and charge–dipole interactions reduce U_B through a charge crowding term $U_C^* \approx c q_i^2/4\pi\epsilon_0\Delta k_B T = c U_B^* q^*/d$, where c is a geometric factor describing the structure of charge clusters adsorbed on the surface (see *Supplementary Note* V-VI; Fig. S7a–b for the full derivation). The crowding term increases with surface charge, where cation accumulation raises the Coulombic potential well, **Fig. 4b**. At sufficiently high surface charge, cation crowding can exceed the surface charge, leading to a charge reversal in the Stern layer (Fig. S8).

Under an external electric field, the adsorbed cations can escape the Coulombic traps of $U_B^* - U_C^*$ via a mechanism that mirrors the Poole–Frenkel effect. In the Poole-Frenkel effect, the applied field lowers the activation energy barrier for carrier release from charge trap sites [29, 30]. The external field tilts the potential energy landscape asymmetrically, decreasing the forward hopping energy barrier by U_H^*, where $E_e = Ecos(\theta)$ and θ is the escape angle (see **Fig. 4.c** and *Supplementary Note* V and Fig. S7c-d for full derivation and potential energy profiles showing field-dependent energy barrier reduction).

Now that we understand the role of field-assisted barrier hopping at the interface, we can propose a functional form $\mathcal{F}$ in Eq. 4. To this end, we revisit Eq. 3, noting that the charge modifies the cation desorption rate from the surface. Therefore, we suggest that the surface term Γ_s be scaled by an additional term that quantifies surface-charge effects. We achieve this by considering $\Gamma_e = exp(U_B^* - U_C^* - U_H^*)$, neglecting the exponentially less probable backward hops. Therefore, we propose the following formula for the average ion drift velocity that works for both charged and charge-neutral pores:

$$\bar{v}_d = \frac{n q_i E D_0}{k_B T}(1 + 2\Gamma_c(1 - \Gamma_s\Gamma_e)) \tag{5}$$

The suggested equation is inherently nonlinear because Γ_e is exponential, and U_H^* depends nonlinearly on E. In the limit of small surface charge, Γ_e tends to 1 so that we recover Eq. 3 for neutral pores.

Fig. 4e shows that, even if we neglect U_C^*, we can adequately capture the nonlinearity and collapse the drift velocities into a master curve. At this stage, we opted to ignore crowding effects to show that complex-ion dynamics can be explained by a single fitting parameter, θ, which we find to lie between $2\pi/5$ and $\pi/2$ for high- and low-ionophilic surfaces, respectively.

D. Superlinear Ion Conductivity Regime Through Interfacial Percolation Networks: Classical interfacial transport theory suggests that mobility is attenuated at ionophilic and charged surfaces [21]. However, our simulations show the opposite behavior at high surface charge and ionophilic surfaces. At sufficiently high external electric fields, we observe that ions move faster at the surface than at the center of the pore (**Fig. 5a,b**). At low ϵ_s^* and weak E, drift velocity profiles follow the classical pattern (see *Supplementary Note* VI, Fig. S9): the maximum drift velocity occurs at the pore center with surface attenuation from hydrodynamic boundaries and interfacial resistance [21]. Increasing ϵ_s^* localizes ions at the pore walls, initially suppressing $\tilde{v_d}$. Beyond a critical ϵ_s^* and E, this trend reverses; surface-adsorbed ions outpace those in the pore center, forming interfacial layers of enhanced mobility. This observation cannot be explained by the trap-and-hop dynamics discussed in the previous section.

To better understand this nonclassical behavior, we computed the interfacial Haven ratio, *i.e.,* the ratio of the apparent self-diffusion coefficient estimated via the conductivity measurement to its actual value, $H_R = D_\sigma/D_T$ (see *Methods* E for calculation details). While H_R values below unity indicate uncorrelated motion, H_R>1 signifies cooperative ion migration [31]. H_R falls below unity at small electric fields but exceeds unity at high E and ϵ_s^*, marking a transition to correlated, collective transport (**Fig.5c,d**). Velocity cross-correlation functions for Na^+–Na^+ and Na^+–H_2O pairs (**Fig. 5e** and *Methods* F) confirm that this regime reflects increasingly collective interfacial motion as ionophilicity and field strength grow. Building on the neutral-surface behavior discussed previously, where interfacial Na^+ is only partially dehydrated and its hydration shell exchanges rapidly ($CN \approx 4.6$–4.9, $\tau_m \approx 15$–54 ps (see *Supplementary Note* IV, Fig. S3)), we now examine how charging the surface reshapes solvation. On charged, ionophilic interfaces, Na^+–-Ow coordination numbers increase toward bulk-like values (up to ≈ 5.35) while water residence times lengthen by nearly two orders of magnitude (up to ≈ 600 ps), indicating long-lived, outer-sphere-dominated complexes with kinetically trapped hydration shells. These persistent, near-bulk hydration structures enable ions to migrate collectively with their hydration cages, producing the correlated ion–water motion and enhanced surface mobility we term interfacial superionicity.

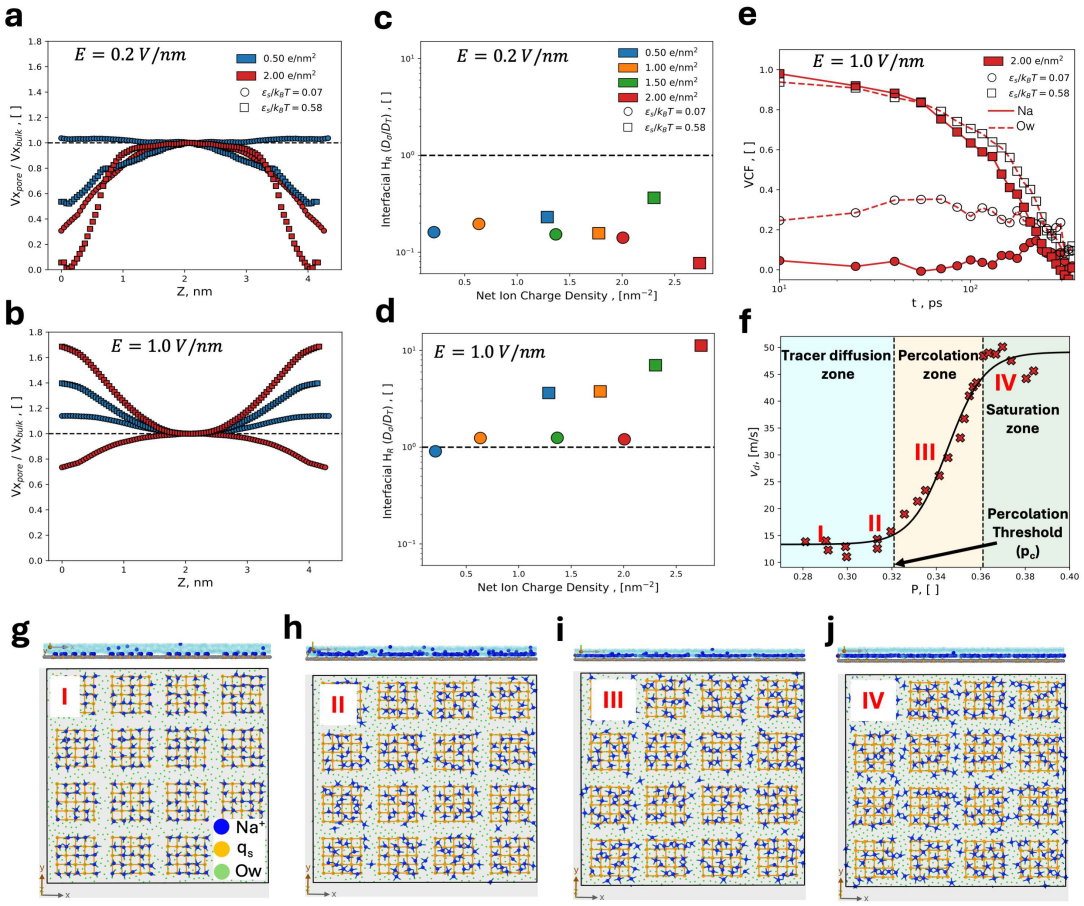


FIG. 5. **Ion crowding and correlated ion transport lead to interfacial superionicity through percolation networks of adsorbed species in the Stern layer.** Normalized drift velocity profiles across pore width at (**a**) low and (**b**) high fields for varying surface charge and ionophilicities show a transition from center-dominated to surface-enhanced mobility. Interfacial Haven ratios H_R capture the shift from (**c**) uncorrelated hopping (H_R<1) to (**d**) collective migration (H_R>1) at high fields and strong ionophilicity. (**e**) Velocity cross-correlation functions for Na^+–Na^+ and Na^+–water at the interface reveal increasing collective motion with increasing ionophilicity. (**f**) The analysis of surface drift velocity versus cluster fraction shows a percolation transition, from transport suppressed by deep traps (regimes I–II) to enhanced conduction along connected networks (regimes II–IV). (**g–j**) Snapshots of the surface–fluid interface show the evolution from isolated ion clusters (I) to growing networks (II–III), and fully percolated transport pathways (IV).

A natural question is whether the altered dielectric permittivity of nanoconfined water contributes to this behavior. Nanoconfinement is known to modify the local dielectric properties of water [32, 33], and prior studies have shown that SPC/E water reproduces these confinement-induced dielectric changes with reasonable accuracy [34]. The in-plane permittivity $\varepsilon_{\parallel}$ can be enhanced near ordered interfacial water layers, which could, in principle, promote ion mobility. To assess this, we computed

$\varepsilon_{\parallel}$ profiles for charged and neutral surfaces at identical ionophilicity (Fig. S10). The charged ionophilic surface, which is precisely the condition producing superionicity, exhibits a suppressed $\varepsilon_{\parallel}$ near the surface relative to the neutral surface of the same ionophilicity. The neutral surface carries higher $\varepsilon_{\parallel}$ yet shows no superionicity. Dielectric enhancement, therefore, cannot account for the observed superionic transport. The suppression of $\varepsilon_{\parallel}$ on the charged surface reflects dense Na^+ accumulation, which displaces interfacial water molecules and disrupts the cooperative dipolar fluctuations responsible for elevated permittivity. Superionicity thus emerges despite an unfavorable dielectric environment, confirming that concerted ion migration through percolation networks is the controlling mechanism.

To better understand the molecular origins of interfacial superionicity, we systematically vary ϵ_s^* at a fixed surface charge density of Σ_s=2.0 e/nm^2. By doing so, we adsorb more ions onto the surface between charge sites and, as a result, increase the percentage of cations that are part of a large network (p) (see *Methods* G for details). Surprisingly, when we plot the average drift velocity as a function of p, we observe a sigmoidal behavior (**Fig. 5f**). This sigmoidal response is reminiscent of those observed in percolation phenomenon. Otherwise stated, the observable p can be viewed as a percolation probability. As shown in **Fig. 5g-j**, increasing ϵ_s^* drives a structural transition from isolated surface clusters (regime I), through cluster growth and coalescence (regimes II–III), to system-spanning percolation networks (regime IV). This percolation transition fundamentally reshapes ion transport. Below the percolation threshold, ions must desorb thermally before axial migration, incurring energetic penalties that suppress mobility. Above this threshold, connected surface networks enable adsorbed ions to migrate cooperatively under strong electric fields, as strong inter-ion correlations sustain collective conduction. This shift explains the non-monotonic dependence of surface conductivity on ϵ_s^*: mobility decreases when traps deepen at low ϵ_s^*, but increases once network connectivity dominates, defining an optimal ϵ_s^* for efficient interfacial ion transport in charged nanopores.

We rationalize the enhanced interfacial ion conductivity by noting that energy barriers to ion transport are reduced (**Fig. 4d**). Cations in percolation networks escape traps and collide with neighboring water molecules and cations, much akin to billiard balls on a pool table. Such collisions motivate us to propose an additional energy term $U_P^* \approx q^2\delta(E)/4\pi\epsilon_0\Delta^2 k_B T$, which lowers the effective energy barriers through correlated ion motion (see *Supplementary Note* VI for full derivation). Hence, the collision effects modify the field-dependent escape probability as follows: $\Gamma_e = \exp(U_B^* - U_C^* - U_H^* - U_P^*)$. We emphasize that the U_P^* contribution appears only above two thresholds: sufficient

surface ion concentration to form connected networks and a critical electric field strong enough to drive correlated migration through collisions. Determining the parameters for calculating U_P^* requires a rigorous analysis of cluster and ion-dipole structures, which is beyond the scope of this study. In view of this, we applied a fitting approach to adjust the coefficients in U_P^* for each surface charge and ionophilicity, as well as for pore size (Table S1).

When all energy barrier modification terms (U_B^*, U_C^*, U_H^*, and U_P^*) are included in Eq. 5, the model accurately predicts average ion drift velocities (inset, **Fig. 4**.e). However, evaluating the percolation correction U_P^* requires fitting multiple model coefficients for each combination of ionophilicity, surface charge, and pore size, raising concerns about overfitting. Future work should replace these empirical fits with physics-based parameterizations by: (i) using explicit cluster-statistics to compute geometric correlation factors directly from ion coordination environments, (ii) performing molecular-dynamics analysis of field-driven hopping trajectories to obtain a predictive relation between ballistic hopping lengths, electric field, and ion packing, and (iii) applying percolation theory to determine the critical surface coverage and field strength that mark the onset of correlated ion transport. Such strategies would consolidate the many fitting coefficients in Table S1 into a smaller set of universal, physically derived quantities.

E. Validation of the Proposed Theoretical Framework: To demonstrate the predictive capability of the proposed theoretical framework, we evaluated its transferability to all-atom simulations. We confine 1 M NaCl electrolyte between atomistically resolved quartz, pyrophyllite, calcite, forsterite (Σ_s= 0.0, 2.0 e/nm^2), and montmorillonite (Σ_s=2.0 e/nm^2) surfaces (see *Methods* A-B for surface and computational details). These minerals preserve native surface terminations, hydration structures, and lattice topographies. When we use the corresponding ϵ_s^* for these surfaces presented in **Fig. 1d-e**, we find that $\tilde{v_d}$ from all-atom simulations collapses onto the same master curve as the reduced-complexity model without adjusting the calibration parameters (**Fig. 6a**). This observation indicates that a single effective surface-interaction strength and surface charge density suffice to encode diverse surface chemistries into pore-scale transport.

We now test the proposed theoretical framework against published experimental data. While validating the theory against interconnected nanoporous media is preferable, natural nanoporous samples contain a mixture of nano-, meso-, and micropores, which makes it difficult to isolate pure nanoscale effects. Thus, we focus on measurements of electrical conductivity in single-pore silicon nitride and carbon nanotubes across multiple electrolytes and pore sizes [18, 35–37]. For pores

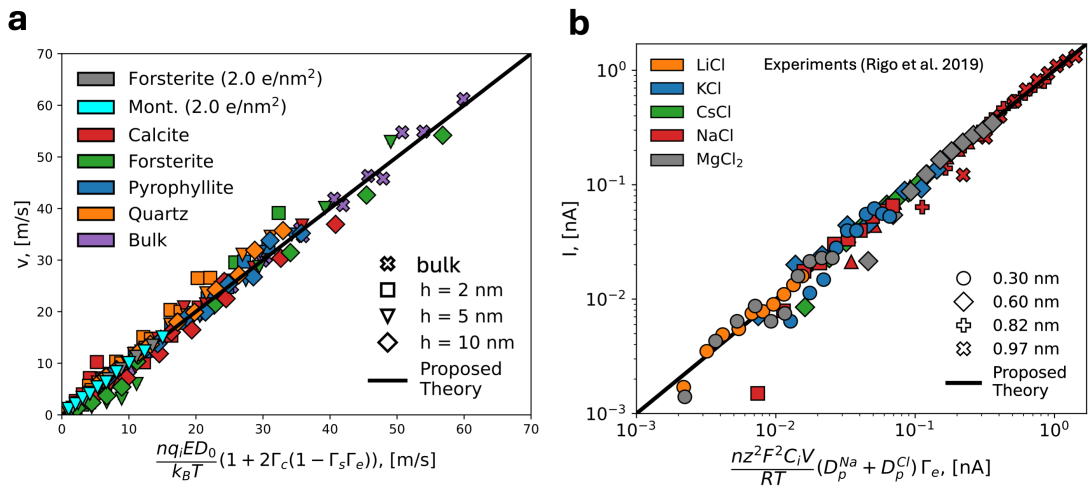


FIG. 6. **The proposed theoretical framework provides a scaling relation that explains ion conductivity in all-atom mineral-electrolyte interface simulations and experimental measurements.** (**a**) Drift velocities from all-atom simulations collapse onto a single master curve when plotted against the theoretical prediction, demonstrating its broad applicability across pore sizes, minerals, and surface charges. (**b**) Experimental currents for multiple electrolytes and nanopore sizes (0.30–0.97 nm) [18] collapse onto the proposed scaling relation, unifying conductivity measurements that originally spanned orders of magnitude in pore size and conductivity space. In this case, the proposed theory was reformulated in terms of current, where z denotes the ion charge magnitude, F is Faraday's constant, V is the applied voltage, C_i denotes the electrolyte concentration, and R is the gas constant.

>100 nm, conductivity approaches the bulk value. Once pores shrink to molecular dimensions, however, conductivity varies by orders of magnitude because ion–surface interactions and disruption of hydration layers dominate bulk-like transport [19, 21] (see Fig. S10a-b). Collapsing this scattered data requires knowledge of D_p, ϵ_s^*, and surface charge parameters for each experimental system, which are not reported for most datasets in the literature. Among the available datasets, Rigo *et al.* [18] report D_p values for sub-nanometer silicon nitride nanopores across multiple electrolytes and pore sizes (0.30–0.97 nm), enabling a direct test of our framework. Fitting Equation 3 to their reported D_p values yields a mean ϵ_s^*=0.57±0.03 that is indicative of an ionophilic surface (see Fig. S10c). After which, fitting the current–voltage curves with Equation 5 recovers a mean surface charge q_s=−0.07±0.05 and trap depth U_B^*=1.6±1.4. With these parameters in hand, the measured currents, which originally spanned orders of magnitude (see Fig. S10b), collapse onto a single unity-slope master curve under the proposed theoretical framework (see **Fig.6b**).

With these validations, the proposed theory establishes a physically grounded, scale-bridging frame-

work for ion conductivity in nanoporous media. Because the model captures molecular-scale interfacial phenomena while naturally recovering bulk electrolyte behavior in the limit of large pore dimensions, it provides a unified constitutive foundation portable across materials and length scales. Such a framework carries far-reaching implications for electrochemical energy storage, water purification and desalination, subsurface and materials characterization, structural health monitoring, and electrokinetic technologies for contaminant remediation and critical mineral recovery.

METHODS

A. Reduced-complexity model: A reduced-complexity surface model captures the key fluid–surface interactions needed to explore a wide range of material chemistries at low cost. We represent each surface as a square lattice of fixed sites separated by 0.1 nm, comparable to typical interatomic spacings in materials and sufficient to resolve the interfacial fluid structure. One surface sheet spans 12 nm by 12 nm and contains 14400 lattice sites. To parameterize the interactions between these idealized sites and electrolyte species, we first analyzed all-atom MD simulations of quartz [0001], pyrophyllite [001], forsterite [010] (Σ_s=0, 2.0 e/nm^2), montmorillonite [001] (Σ_s=2.0 e/nm^2), and calcite [10$\bar{1}$4]. These surfaces exhibit different terminations and hydro/ionophilic properties that span the spectrum of material-electrolyte interactions.

In the reduced-complexity model, we represent fluid–surface interactions using Lennard–Jones potentials with parameter ϵ_s. To link ϵ_s in the reduced-complexity model to all-atom simulations, we compared their density profiles ρ_z. For each material, we identified the upper and lower envelopes of the main interfacial density peak for ions and water (Ow). We subsequently adjusted $\epsilon_{\text{Ow-s}}$ and $\epsilon_{\text{ion-s}}$ until both the peak height and position in the reduced model matched the atomistic results. Finally, we linearly interpolated between the calibrated ϵ_s values to obtain a continuous parameter space spanning the full range of interfacial behaviors observed in all-atom simulations. Together, the calibrated ϵ_s values span $\epsilon_{\text{Na-s}}$=0.18-1.45 kJ/mol, $\epsilon_{\text{Cl-s}}$=0.09-0.70 kJ/mol, and $\epsilon_{\text{Ow-s}}$=0.21-0.80 kJ/mol (see Table S2 for the list of all simulation parameters).

B. Computational approach: We performed all molecular dynamics simulations in GROMACS using slit-pore geometries constructed from the reduced-complexity model. The slit pores contained 2088–42544 water molecules, 45–1344 Na^+, and 45–768 Cl^- ions, depending on the pore size, surface ionophilicity, and surface charge. We modeled the solvent as SPC/E water [38]. SPC/E water is known to reproduce confinement-induced dielectric behavior in slit nanopore geometries [34]. The altered permittivity environment under nanoconfinement is therefore implicitly captured in our simulations without requiring an explicit dielectric model. NaCl as Dang–Smith [39], and other electrolytes as the Kirkwood–Buff force field for alkali halides [40]. Montmorillonite and forsterite were modeled as ClayFF [41] and a modified ClayFF parameterization [42], respectively. We model calcite as the Raiteri–Gale [43], and quartz as the silica force field and surface model database [44]. We set up 1 M NaCl electrolyte solutions with additional setups for KCl, KF, $CaCl_2$, and $MgCl_2$ to study cation-

and anion-specific effects on confined transport. Equilibration was carried out in the NPT ensemble at 300 K and 1 bar for 1 ns, followed by NVT production runs at 300 K. The equations of motion were integrated with a 1 fs time step using the leap-frog/velocity-Verlet scheme and a Verlet cutoff of 1.0 nm for Lennard–Jones and real-space Coulomb interactions. Long-range electrostatics were treated with the Particle Mesh Ewald using fourth-order interpolation and a real-space grid spacing of 0.16 nm.

Periodic boundary conditions were applied in all three directions, with rigid or position-restrained solid slabs along z to prevent slab deformation. A 10 nm vacuum gap above and below the slabs removed spurious slab–slab electrostatic interactions along z. Temperature was controlled using a velocity-rescale thermostat applied separately to the solid and fluid groups, with a relaxation time of 0.1 ps for the mobile fluid and no coupling for the restrained solid atoms. Bond constraints involving hydrogen were treated with LINCS (order 4), and long-range dispersion corrections were applied to recover accurate densities and pressures under nanoconfinement. Ionic transport under confinement was quantified using two protocols. Zero-field NVT simulations of 20 ns provided in-plane diffusion coefficients from mean-squared displacement analysis. Constant electric fields of 0.1–1.0 V/nm were then applied along the x-direction to drift ions, and average drift velocities were obtained from 2 ns production runs, with selected 20 ns simulations used to confirm convergence. Drift velocities were computed from ensemble-averaged displacements along the field direction, $\tilde{v_d} = \langle \Delta r_x \rangle / \Delta t$.

C. Diffusion coefficient analysis: Initial attempts to extract pore diffusion coefficient, D_p, values from MD trajectories yielded a paradoxical result: confined ions appeared to diffuse faster than in bulk solution, contradicting the intuition that confinement should hinder transport (see *Supplementary Note* II, Fig. S11). This anomaly was traced to hydrodynamic artifacts from the finite simulation cell and periodic boundary conditions [27]. Spurious hydrodynamic coupling between periodic images biased the measured diffusion coefficients upward. We performed systematic finite-size scaling to resolve this artifact by increasing the lateral simulation box size from 3 nm to 12 nm. We subsequently extrapolated the results to infinite lateral dimensions to obtain size-effect-corrected D_p values. All subsequent drift simulations used 12 nm lateral dimensions to ensure that transport coefficients converged and remained physically meaningful.

From the mean-square displacement (MSD) using Einstein's relation, we calculated parallel (xy-plane) diffusion coefficients under zero electric field conditions as:

$$D_{xy} = \lim_{t\to\infty} \frac{\langle |r_{xy}(t) - r_{xy}(0)|^2 \rangle}{4t} \tag{6}$$

Because diffusion in the z-direction was negligible under strong confinement, the effective three-dimensional diffusion coefficient entering the Nernst-Einstein relation was approximated as $D_{eff} = nD_{xy}$, where n (n=2/3 for H>1 nm and n=1/3 for $H \leq 1$ nm) accounts for the reduced dimensionality while maintaining consistency with drift velocity measurements along the x-axis under applied fields.

D. Van Hove space-time correlation analysis: We characterized the single-particle dynamics of surface-adsorbed ions using the self part of the van Hove space-time correlation function,

$$G_s(r,t) = \frac{1}{N}\sum_{i=1}^{N} \langle \delta\left[r - |r_i(t) - r_i(0)|\right] \rangle \tag{7}$$

where N is the number of ions that remain within the first interfacial layer throughout a given observation window, $r_i(t)$ is the position of ion i at time t, and the average is taken over ions and time origins. To resolve the evolution from vibrational motion to long-time transport, $G_s(r,t)$ was evaluated at lag times t=20,30,…,90 ps, and only ions that continuously resided in the interfacial layer over each corresponding time interval were included in the statistics. This restricted self-part therefore reports the displacement statistics of ions that survive at the surface over the full observation time, enabling direct identification of hopping-like behavior.

E. Interfacial Haven ratio analysis: The Haven's ratio (H_R) is defined as the ratio of collective (conductive-based) to tracer (diffusivity-based) mobility. We quantified ion correlations by evaluating H_R for ions in the first interfacial layer (0.3 nm thick). Here, we employed the survival-probability mean-squared-displacement formulation of Liu *et al.*[45] to calculate the tracer diffusion coefficient D_T of surface-adsorbed ions as:

$$D_T = \lim_{\tau\to\infty} \frac{\frac{1}{T}\sum_{t=1}^{T} \frac{1}{N(t)} \sum_{i\in S(t,t+\tau)} (x_i(t+\tau) - x_i(t))^2}{2\tau \left(\frac{1}{T}\sum_{t=1}^{T} \frac{N(t,t+\tau)}{N(t)}\right)} \tag{8}$$

where $S(t, t+\tau)$ designate the set of all ions that stay in the interfacial layer, T is the total number of time steps, $N(t)$ is the number of particles in the interfacial region at time t, and $N(t, t+\tau)$ is the number of particles that remain in the region during the interval $[t,\ t+\tau]$. The effective diffusion coefficient inferred from conductivity was evaluated using the Nernst-Einstein relation $D_\sigma = v_d k_B T/(qE)$, where v_d is the drift velocity of ions at the surface. We therefore compute the Haven ratio as $H_R = D_\sigma/D_T$.

F. Velocity cross correlation analysis: We restricted the velocity cross-correlation analysis to ions that remained adsorbed at the charged surface for a statistically meaningful residence time. For

each species, only ions whose continuous residence within the first interfacial layer (0.3 nm) persisted for at least 350 ps were included, ensuring that the statistics selectively probe the dynamics of long-lived surface-adsorbed ions rather than transiently visiting particles. We evaluated the velocity cross-correlation function between species i and j as:

$$\langle v_i(0) \cdot v_j(t) \rangle = \frac{1}{N_i N_j} \sum_{k=1}^{N_i} \sum_{l=1}^{N_j} \langle v_{i,k}(0) \cdot v_{j,l}(t) \rangle \tag{9}$$

where $v_{i,k}(t)$ is the velocity of particle k of species i at time t, N_i and N_j are the numbers of surface-surviving particles of species i and j, respectively, and the angular brackets denote time averaging over the production trajectories. Cross-correlations were computed for ion–ion and ion–water pairs within the interfacial layer to quantify the degree of correlated migration among these long-lived adsorbed species.

G. Percolation calculation: We used a lattice-based cluster identification of hydrated Na^+ at the charged surface to analyze percolation of interfacial hydration structures. We equilibrated a simplified charged slab with surface charge density Σ_s=2.0 e/nm^2 with approximately six water layers and neutralized with Na^+ counterions. We tuned the surface hydro/ionophilicity by varying the ion/water-surface interaction strength ϵ_s from 0.01 to 3.5 kJ/mol to span the hydrophobic-hydrophilic transition. Under an applied electric field of E=1.0 V/nm, we defined interfacial clusters from Na^+–Ow connectivity within a cutoff of r_c=0.29 nm, representing the minimum after the first peak in the radial distribution function. We then calculate the percolation cluster fraction, P, as follows: for a given trajectory frame i, let $N_{\mathrm{Na}}(i)$ and $N_{\mathrm{W}}(i)$ denote the numbers of Na^+ and water oxygen atoms, respectively, within the interfacial slab, and let $r_{jk}(i)$ be the distance between Na^+ atom j and water oxygen atom k in that frame. A Na^+–Ow pair (j,k) is considered connected if $r_{jk}(i) \leq r_c$. Then, we count the total number of atoms participating in at least one Na^+-water contact in frame i, as $N_{clust}(i)$. If we divide this number by the total number of atoms in the Stern layer and average it over all independent trajectory frames, we obtain the P parameter.

REFERENCES

[1] P. Simon and Y. Gogotsi, Materials for electrochemical capacitors, Nature materials **7**, 845 (2008).

[2] M. R. Lukatskaya, S. Kota, Z. Lin, M.-Q. Zhao, N. Shpigel, M. D. Levi, J. Halim, P.-L. Taberna, M. W.

Barsoum, P. Simon, *et al.*, Ultra-high-rate pseudocapacitive energy storage in two-dimensional transition metal carbides, in *MXenes* (Jenny Stanford Publishing, 2023) pp. 723–743.

[3] C. Merlet, B. Rotenberg, P. A. Madden, P.-L. Taberna, P. Simon, Y. Gogotsi, and M. Salanne, On the molecular origin of supercapacitance in nanoporous carbon electrodes, Nature materials **11**, 306 (2012).

[4] S. Porada, R. Zhao, A. van der Wal, V. Presser, and P. M. Biesheuvel, Review on the science and technology of water desalination by capacitive deionization, Progress in materials science **58**, 1388 (2013).

[5] K. Zuo, S. Garcia-Segura, G. A. Cerrón-Calle, F.-Y. Chen, X. Tian, X. Wang, X. Huang, H. Wang, P. J. Alvarez, J. Lou, *et al.*, Electrified water treatment: fundamentals and roles of electrode materials, Nature Reviews Materials **8**, 472 (2023).

[6] N. R. Aluru, F. Aydin, M. Z. Bazant, D. Blankschtein, A. H. Brozena, J. P. de Souza, M. Elimelech, S. Faucher, J. T. Fourkas, V. B. Koman, *et al.*, Fluids and electrolytes under confinement in single-digit nanopores, Chemical reviews **123**, 2737 (2023).

[7] H. Fan, Y. Huang, and N. Y. Yip, Advancing ion-exchange membranes to ion-selective membranes: principles, status, and opportunities, Frontiers of Environmental Science & Engineering **17**, 25 (2023).

[8] P. Marchetti, M. F. Jimenez Solomon, G. Szekely, and A. G. Livingston, Molecular separation with organic solvent nanofiltration: a critical review, Chemical reviews **114**, 10735 (2014).

[9] H. Xiao, Y. Feng, W. R. Goundry, and S. Karlsson, Organic solvent nanofiltration in pharmaceutical applications, Organic Process Research & Development **28**, 891 (2024).

[10] A. Revil and P. Leroy, Constitutive equations for ionic transport in porous shales, Journal of Geophysical Research: Solid Earth **109** (2004).

[11] D. Chung, A critical review of electrical-resistance-based self-sensing in conductive cement-based materials, Carbon **203**, 311 (2023).

[12] A. Binley, S. S. Hubbard, J. A. Huisman, A. Revil, D. A. Robinson, K. Singha, and L. D. Slater, The emergence of hydrogeophysics for improved understanding of subsurface processes over multiple scales, Water resources research **51**, 3837 (2015).

[13] A. Revil, M. Le Breton, Q. Niu, E. Wallin, E. Haskins, and D. Thomas, Induced polarization of volcanic rocks–1. surface versus quadrature conductivity, Geophysical Journal International **208**, 826 (2017).

[14] A. Einstein, Über die von der molekularkinetischen theorie der wärme geforderte bewegung von in ruhenden flüssigkeiten suspendierten teilchen, Annalen der physik **4** (1905).

[15] J. Chmiola, G. Yushin, Y. Gogotsi, C. Portet, P. Simon, and P.-L. Taberna, Anomalous increase in carbon capacitance at pore sizes less than 1 nanometer, science **313**, 1760 (2006).

[16] S. Fleischmann, Y. Zhang, X. Wang, P. T. Cummings, J. Wu, P. Simon, Y. Gogotsi, V. Presser, and V. Augustyn, Continuous transition from double-layer to faradaic charge storage in confined electrolytes,

Nature Energy **7**, 222 (2022).

[17] Y. Li, Z. Li, F. Aydin, J. Quan, X. Chen, Y.-C. Yao, C. Zhan, Y. Chen, T. A. Pham, and A. Noy, Water-ion permselectivity of narrow-diameter carbon nanotubes, Science advances **6**, eaba9966 (2020).

[18] E. Rigo, Z. Dong, J. H. Park, E. Kennedy, M. Hokmabadi, L. Almonte-Garcia, L. Ding, N. Aluru, and G. Timp, Measurements of the size and correlations between ions using an electrolytic point contact, Nature communications **10**, 2382 (2019).

[19] D. Stein, M. Kruithof, and C. Dekker, Surface-charge-governed ion transport in nanofluidic channels, Physical Review Letters **93**, 035901 (2004).

[20] Y. Green, Ion transport in nanopores with highly overlapping electric double layers, The Journal of Chemical Physics **154** (2021).

[21] R. B. Schoch, J. Han, and P. Renaud, Transport phenomena in nanofluidics, Reviews of modern physics **80**, 839 (2008).

[22] Y. Noh and N. R. Aluru, Ion transport in electrically imperfect nanopores, ACS Nano **14**, 10518 (2020).

[23] X. Liu, Y. Song, W. Geng, H. Li, L. Xiao, and W. Wu, Fast and selective fluoride ion conduction in sub-1-nanometer metal-organic framework channels, Nature Communications **10**, 2490 (2019).

[24] N. Kavokine, R. R. Netz, and L. Bocquet, Fluids at the nanoscale: From continuum to subcontinuum transport, Annual Review of Fluid Mechanics **53**, 377 (2021).

[25] P.-A. Cazade, R. Hartkamp, and B. Coasne, Structure and dynamics of an electrolyte confined in charged nanopores, The Journal of Physical Chemistry C **118**, 5061 (2014).

[26] A. Saugey, L. Joly, C. Ybert, J.-L. Barrat, and L. Bocquet, Diffusion in pores and its dependence on boundary conditions, Journal of Physics: Condensed Matter **17**, S4075 (2005).

[27] P. Simonnin, B. Noetinger, C. Nieto-Draghi, V. Marry, and B. Rotenberg, Diffusion under confinement: Hydrodynamic finite-size effects in simulation, Journal of chemical theory and computation **13**, 2881 (2017).

[28] W. Sparreboom, A. van den Berg, and J. C. Eijkel, Principles and applications of nanofluidic transport, Nature nanotechnology **4**, 713 (2009).

[29] J. Frenkel, On pre-breakdown phenomena in insulators and electronic semi-conductors, Physical Review **54**, 647 (1938).

[30] J. G. Simmons, Generalized formula for the electric tunnel effect between similar electrodes separated by a thin insulating film, Journal of applied physics **34**, 1793 (1963).

[31] A. Marcolongo and N. Marzari, Ionic correlations and failure of nernst-einstein relation in solid-state electrolytes, Physical Review Materials **1**, 025402 (2017).

[32] A. Chogani, H. E. King, B. Tutolo, A. Živković, and O. Plümper, Geochemistry of lithospheric aqueous

fluids modified by nanoconfinement, Nature Geoscience **18**, 191 (2025).

[33] R. Wang, M. Souilamas, A. Esfandiar, R. Fabregas, S. Benaglia, H. Nevison-Andrews, Q. Yang, J. Normansell, P. Ares, G. Ferrari, *et al.*, In-plane dielectric constant and conductivity of confined water, Nature **646**, 606 (2025).

[34] A. Schlaich, E. W. Knapp, and R. R. Netz, Water dielectric effects in planar confinement, Physical review letters **117**, 048001 (2016).

[35] D. C. Martinez Casillas, M. P. Longinotti, M. M. Bruno, F. Vaca Chavez, R. H. Acosta, and H. R. Corti, Diffusion of water and electrolytes in mesoporous silica with a wide range of pore sizes, The Journal of Physical Chemistry C **122**, 3638 (2018).

[36] S. W. Kowalczyk, A. Y. Grosberg, Y. Rabin, and C. Dekker, Modeling the conductance and dna blockade of solid-state nanopores, Nanotechnology **22**, 315101 (2011).

[37] S. Balme, F. Picaud, M. Manghi, J. Palmeri, M. Bechelany, S. Cabello-Aguilar, A. Abou-Chaaya, P. Miele, E. Balanzat, and J. M. Janot, Ionic transport through sub-10 nm diameter hydrophobic high-aspect ratio nanopores: experiment, theory and simulation, Scientific reports **5**, 10135 (2015).

[38] H. J. Berendsen, J.-R. Grigera, and T. P. Straatsma, The missing term in effective pair potentials, Journal of Physical Chemistry **91**, 6269 (1987).

[39] D. E. Smith and L. X. Dang, Computer simulations of nacl association in polarizable water, The Journal of Chemical Physics **100**, 3757 (1994).

[40] M. B. Gee, N. R. Cox, Y. Jiao, N. Bentenitis, S. Weerasinghe, and P. E. Smith, A kirkwood-buff derived force field for aqueous alkali halides, Journal of chemical theory and computation **7**, 1369 (2011).

[41] R. T. Cygan, J.-J. Liang, and A. G. Kalinichev, Molecular models of hydroxide, oxyhydroxide, and clay phases and the development of a general force field, The Journal of Physical Chemistry B **108**, 1255 (2004).

[42] S. Kerisit, E. J. Bylaska, and A. R. Felmy, Water and carbon dioxide adsorption at olivine surfaces, Chemical Geology **359**, 81 (2013).

[43] P. Raiteri, J. D. Gale, D. Quigley, and P. M. Rodger, Derivation of an accurate force-field for simulating the growth of calcium carbonate from aqueous solution: A new model for the calcite- water interface, The Journal of Physical Chemistry C **114**, 5997 (2010).

[44] F. S. Emami, V. Puddu, R. J. Berry, V. Varshney, S. V. Patwardhan, C. C. Perry, and H. Heinz, Force field and a surface model database for silica to simulate interfacial properties in atomic resolution, Chemistry of Materials **26**, 2647 (2014).

[45] P. Liu, E. Harder, and B. Berne, On the calculation of diffusion coefficients in confined fluids and interfaces with an application to the liquid- vapor interface of water, The Journal of Physical Chemistry B **108**,

519 6595 (2004).

520 ACKNOWLEDGEMENTS

521 We thank the Center for Understanding Subsurface Signals and Permeability (CUSSP) team for
522 their collaborative support and scientific insights that were essential to this work. We also acknowledge
523 the computational resources provided by the University of California, Irvine HPC3 cluster and the as-
524 sociated support staff, as well as the National Energy Research Scientific Computing Center (NERSC),
525 a U.S. Department of Energy Office of Science User Facility, for additional high-performance com-
526 puting resources.

527 ***Funding:*** This research was funded by the U.S. Department of Energy (DOE), Office of Science
528 under FWP 81834.

529 ***Author Contributions:*** M.J.A.Q., K.M.R., and R.L.D. designed the research. J.P.O. devel-
530 oped the large-scale computational framework for the parameter space, performed molecular dynam-
531 ics simulations, and gathered the simulation results. J.P.O analysed the statistical components of
532 the results. J.P.O. and M.J.A.Q. developed the theoretical framework using dimensional analysis.
533 J.P.O. and M.J.A.Q. wrote the initial draft of the manuscript, and other authors edited and provided
534 comments that enriched the final draft of the manuscript.

535 ***Competing Interests:*** The authors declare no competing interests.

536 ***Data Availability:*** All simulation and experimental results are shown in detail in the main
537 article and the accompanying Supplementary Information. The simulations were performed using
538 standard open-source molecular dynamics software, GROMACS v.2024.2. The input files used for
539 the GROMACS simulations, as well as the diffusion and drift velocity results, are publicly available
540 on Zenodo at https://doi.org/10.5281/zenodo.19055862.

541 FIGURE LEGEND AND CAPTIONS

542 **Figure 1: A multiscale framework for ion conductivity in nanoporous media**. When
543 an external electric field is applied to (**a**) mesoporous media, (**b**) ions preferentially migrate, re-
544 sulting in an effective electric current. To capture the nanofluidic transport regimes, we set up (**c**)
545 reduced-complexity MD simulations, in which confined electrolyte species are atomistically resolved
546 between idealized surfaces that engender ionophilicity and surface charge. The dark gray balls are

coarse-grained surface species, red balls are oxygen, white represents hydrogen, navy blue shows sodium, and green identifies chlorine ions. By systematically varying the ionophilicity parameter, we can adjust the (**d**) Maximum interfacial water and Na^+ densities. We find (**e**) coarse-grained and all-atom simulations give consistent Na^+ surface densities across neutral and charged surfaces, indicating that ionophilicity and charge capture the essential surface chemistry. In the inset images, gray represents aluminum, dark gray represents carbon, lemon green represents magnesium, orange represents silicon, blue represents calcium, and electrolyte species are shown as before.

Figure 2: Ion transport in charge-neutral nanopores follows an ohmic behavior that breaks the Nernst-Einstein relation. (**a**) Drift velocities from all reduced-complexity simulations show significant scatter across pore sizes and surface ionophilicities but remain strictly linear with respect to the applied external electric field. These pore size and ionophilicity effects are essentially reflected in (**b**) pore diffusion coefficients that match our theoretical predictions for different ion types. Our proposed ion conductivity theoretical framework collapses the average drift velocities for all pore sizes and surface affinities onto a master curve for (**c**) NaCl electrolyte and (**d**) other electrolytes, confirming the broad application of the proposed scaling relationship.

Figure 3: Cation transport in negatively charged nanopores follows a nonlinear behavior characterized by a hopping mechanism between surface trap sites. This nonlinearity increases with ϵ_s^* and Σ_s for the average drift velocity versus the electric field. It becomes less noticeable for (a) low ionophilicity, ϵ_s^*=0.07, but more pronounced for (b) high ionophilicity, ϵ_s^*=0.58. The Van Hove space-time correlation reveals the molecular origins of this hopping mechanism, $G_s(r,t)$, where (c) charged-neutral pores exhibit smooth Gaussian profiles indicative of continuous diffusive motion and (d) charged pores show distinct peaks at characteristic hopping distances signaling a transition to trap-assisted transport.

Figure 4: The energy barrier landscape of adsorbed ions on trap sites is at the origins of the observed nonlinear ion transport mechanisms. (a) Surface charge sites create electrostatic traps of depth U_B that immobilize counterions. (b) At sufficiently large surface charges, charge-charge and charge-dipole crowding reduce the effective trap depth by U_C. (c) An applied electric field tilts the energy barrier potential in the direction of the applied field and lowers the

forward barrier by U_H, promoting field-assisted escape. (d) Collective ion-ion correlations in percolation networks further reduce barriers by U_P, enabling rapid lateral transport along connected pathways. At the limit of negligible ion crowding and correlation effects (e), the proposed theoretical framework for charged surfaces accurately collapses average drift velocities onto the unity line. The inset shows the perfect fit when crowding and ion-correlation effects are accounted for (see discussion in *Supplementary Note* V.

Figure 5: Ion crowding and correlated ion transport lead to interfacial superionicity through percolation networks of adsorbed species in the Stern layer. Normalized drift velocity profiles across pore width at (**a**) low and (**b**) high fields for varying surface charge and ionophilicities show a transition from center-dominated to surface-enhanced mobility. Interfacial Haven ratios H_R capture the shift from (**c**) uncorrelated hopping (H_R<1) to (**d**) collective migration (H_R>1) at high fields and strong ionophilicity. (**e**) Velocity cross-correlation functions for Na^+–Na^+ and Na^+–water at the interface reveal increasing collective motion with increasing ionophilicity. (**f**) The analysis of surface drift velocity versus cluster fraction shows a percolation transition, from transport suppressed by deep traps (regimes I–II) to enhanced conduction along connected networks (regimes II–IV). (**g**–**j**) Snapshots of the surface–fluid interface show the evolution from isolated ion clusters (I) to growing networks (II–III), and fully percolated transport pathways (IV).

Figure 6: The proposed theoretical framework provides a scaling relation that explains ion conductivity in all-atom mineral-electrolyte interface simulations and experimental measurements. (**a**) Drift velocities from all-atom simulations collapse onto a single master curve when plotted against the theoretical prediction, demonstrating its broad applicability across pore sizes, minerals, and surface charges. (**b**) Experimental currents for multiple electrolytes and nanopore sizes (0.30–0.97 nm) [18] collapse onto the proposed scaling relation, unifying conductivity measurements that originally spanned orders of magnitude in pore size and conductivity space. In this case, the proposed theory was reformulated in terms of current, where z denotes the ion charge magnitude, F is Faraday's constant, V is the applied voltage, C_i denotes the electrolyte concentration, and R is the gas constant.

Supplementary Files

This is a list of supplementary files associated with this preprint. Click to download.

- SInanoscale.pdf